Journal of Statistical Physics, Vol. 81, Nos. 1/2, 1995

Three-Dimensional Immiscible Lattice Gas: Application to Sheared Phase Separation

John F. Olson[1] **and Daniel H. Rothman**[1]

Received December 12, 1994; final March 21, 1995

A new lattice-gas cellular automaton model for simulating binary fluids in three dimensions is introduced. It is particularly suitable for modeling slow flows of mixtures with complicated interface geometries or within complicated boundaries, such as in the interior of a porous rock. Phase separation is triggered spontaneously in the model by statistical fluctuations and phase domains are approximately isotropic. The measured surface tension is large compared to that in analogous two-dimensional models. The model is applied to a study of the time-dependent effective viscosity of a phase-separating mixture in a simple shear flow. Results qualitatively match both experiment and theory: the viscosity increases rapidly, then decays gradually to a steady-state value which is larger than the viscosity of the pure fluids. The effective viscosity increases with increasing concentration and decreases with increasing strain rate.

KEY WORDS: Multiphase flow; computational techniques; phase transitions.

1. INTRODUCTION

A vinaigrette is a binary fluid mixture; so is a cloud, consisting of drops of water suspended in air. An oil reservoir usually contains gas or water or both along with the oil, so it is better to describe it as a multiphase mixture dispersed among the grains of a sedimentary rock rather than as a single phase. An alloy or a polymer blend may separate into phases as it cools, leading to properties different from its components; indeed, the effective properties of such mixtures are of considerable technological importance.(1) These are just a few examples of commonplace multiphase fluid mixtures; despite their ubiquity and the relative simplicity of the constituent phases,

---

[1] Department of Earth, Atmospheric and Planetary Sciences, Massachusetts Institute of Technology, Cambridge, Massachusetts 02139.

and despite a long history of theoretical and empirical study (for example, refs. 2–10), their rheological properties remain poorly understood. While analytical methods have yielded much insight, practical experimental systems are often more complicated than the theory. Numerical methods provide a means to extend the theory to these more complex systems or, conversely, to make the complexity of real systems more available to theoretical analysis.

The equations of motion for fluid mixtures are well known: the Navier–Stokes equations describe the fluid away from interfaces, while the specification of "jump" boundary conditions describes the coupling of interfaces to the bulk fluid.(11) Applying boundary conditions at interfaces which are continually moving, merging, and breaking is difficult in analytical work, so a variety of numerical methods have been developed. These include the volume-of-fluid (VOF),(12) cell-dynamical system (CDS),(13, 14) lattice-gas(15–18) and lattice-Boltzmann(19–23) methods. Each of these methods has advantages for different kinds of calculations. The VOF method offers flexibility, although it is apparently inapplicable for modeling the early stages of phase separation; the CDS method is designed for modeling these early stages, but does not conveniently incorporate hydrodynamic phenomena; the lattice-Boltzmann method can model early phase separation efficiently and naturally incorporates hydrodynamics, but fluctuations, which are essential for initiating spinodal decomposition, must be imposed on the model by fiat. The lattice gas has the advantages of the lattice-Boltzmann method, and it is inherently faster; further, it has fluctuations which on the one hand trigger spinodal decomposition, but on the other, obscure detailed flow structure. The averaging needed to reduce the noise so that details may be resolved may eliminate the speed advantage, but if one wishes to calculate a single macroscopic property, such as the effective viscosity of a mixture, spatial averaging may be sufficient and speed is regained. In addition, the Boolean lattice gas may be simulated on existing special-purpose hardware, notably CAM-8,(24, 25) which may provide substantial increases in speed. In this paper, a new lattice-gas cellular automaton method for modeling binary fluid mixtures in three dimensions is described and applied to a study of the time-dependent rheology of sheared, phase-separating systems.(26–28)

Two main technical innovations have been incorporated into our new model. First, a symmetric discretization scheme for the interface orientation makes the tables needed for efficient calculations compact enough to be practical; second, a new scheme is introduced (called the "dumbbell method") for modifying the stress tensor at interfaces to create surface tension. A three-dimensional, immiscible lattice-gas cellular automaton had been developed earlier(29) using different ideas; however, our new model is more closely related to well-studied lattice-gas and lattice-Boltzmann models of immiscible fluids(15, 18–20, 30) and accordingly we feel that its theoretical foundation is better understood. Perhaps even more importantly, our new model offers the possibility of a relatively simple extension to three or more phases, for which there are now only two-dimensional lattice-gas models.(31, 32)

In what follows, a brief description of lattice-gas models will be made, emphasizing the discreteness of all the state variables and operations in such models. The new model will be introduced by adding another property to the existing three-dimensional, single-species lattice gas, a *color* which labels each particle; the dynamics is then modified by adding two new operations which depend on the distribution of color. These operations are *reorienting*, which employs the dumbbell method to generate surface tension between the species, and *recoloring*, which arranges the colors of the particles so that the two species separate from one another. Both these operations depend on the orientation of interfaces between the species, so both require the symmetric discretization scheme mentioned above.

After describing the method itself, we present certain properties of the model. Uniform mixtures are shown to separate into distinct phases, and the surface tension in the model is found to satisfy Laplace's law, which serves both as a test of the model and as a means to measure the strength of the surface tension. The surface tension is found to be much stronger than had been observed in earlier two-dimensional models and phase domains are additionally shown to be statistically isotropic. Lastly, the lattice gas is used to model a binary mixture undergoing phase separation during a steady shear flow, and the time-dependent effective viscosity of the mixture is measured. The viscosity is observed to increase rapidly after the separation starts and then to decay more gradually to a steady-state viscosity which is larger than that of the pure fluids. This qualitatively matches experimental observations, and is also shown to be consistent with theory.

2. LATTICE GAS MODELS

The lattice-gas method, as proposed by Frisch *et al.*,(33, 34) models fluids not by solving discretized Navier–Stokes equations, but by simulating in a grossly simplified way the interactions of particles composing the fluid. These particles should be understood not as simplified molecules, but as a metaphor, since their properties are entirely abstract and do not reflect those of real particles composing real fluids. Nevertheless, the equations of hydrodynamics can be recovered from the average motions of these particles.

Lattice-gas methods have been described many times in the literature (for example, refs. 34 and 18), so only a very brief description will be given here. A single-phase lattice gas is fully discrete in time, space, mass, and velocity. Its particles occupy nodes of a regular, space-filling lattice and move from one node to another in each time step. A particle usually has only one property, a velocity $\mathbf{c}$ which is exactly enough to move it from one node to a neighbor in one time step. Because the lattice is regular, the set of all possible velocities is finite and the same set suffices for every node. The set can be indexed in any convenient way. The particles have a Fermi exclusion rule: no two particles may have the same velocity at the same node at the same time. Therefore, the presence or absence of a particle with velocity $\mathbf{c}_i$ can be indicated with the state of a single bit: $n_i(\mathbf{x}, t) = 1$ if a particle with velocity $\mathbf{c}_i$ is present at the node located at $\mathbf{x}$ at time step t, and 0 otherwise. The *state* of a node is the set of all the n_i, and will be denoted $\mathbf{n}$.

The particles undergo two operations, *propagation* and *collision*, in each time step. The particles present at a node collide with each other, conserving the number of particles and the total momentum at the node, but assigning new velocities to the particles; symbolically,

$$\mathbf{n}'(\mathbf{x}, t) = \mathscr{C}(\mathbf{n}(\mathbf{x}, t)) \tag{1}$$

where $\mathscr{C}$ is the *collision operator*, a function which maps the set of all states onto itself, satisfying the conservation properties specified above. After the collision, each particle propagates to the neighboring node in the direction of its velocity:

$$n_i(\mathbf{x} + \tau\mathbf{c}_i, t + \tau) = n'_i(\mathbf{x}, t) \tag{2}$$

where τ is the duration of a time step. In what follows, τ will be taken to be 1, and $\mathbf{c}_i$ will be used interchangeably as a velocity or as a displacement. A coarse-grained average of the particle velocities $\mathbf{u}$, satisfies equations much like the Navier–Stokes equations for incompressible fluids(33–37, 18):

$$\nabla \cdot \mathbf{u} = 0 \qquad \text{and} \qquad \rho \frac{\partial \mathbf{u}}{\partial t} + \rho g(\rho) \mathbf{u} \cdot \nabla \mathbf{u} = -\nabla P + \eta \nabla^2 \mathbf{u} \tag{3}$$

where P is pressure, η is dynamic viscosity, and ρ is the density of the fluid. If the factor $g(\rho)$, which is a consequence of the discreteness of the lattice, were equal to one, these would be precisely the Navier–Stokes equations. For single-phase models, the factor $g(\rho)$ can be eliminated by rescaling the velocity,(33) and more involved methods exist to make $g(\rho)$ equal to one in two-phase fluids(38), but for low-Reynolds-number flow (as will be considered in this paper) $g(\rho)$ is of little consequence.

In order to have isotropic dissipation in three dimensions, the nodes of the lattice are chosen to be members of a "face-centered hypercubic" (FCHC) lattice,(39) a four-dimensional lattice of polytopes with Schläfli symbol $\{3, 4, 3\}$.(40) Although this lattice is connected in four dimensions, it can effectively be projected into three dimensions by making it only two nodes thick and periodic in the fourth dimension. Figure 1 shows a three-dimensional projection of the unit cell of the lattice. Each node is connected to 24 identical nearest neighbors, and the velocities are vectors with two coordinates zero and two coordinates equal to ± 1. The lattice can be described as the set of points with four integer Cartesian coordinates which

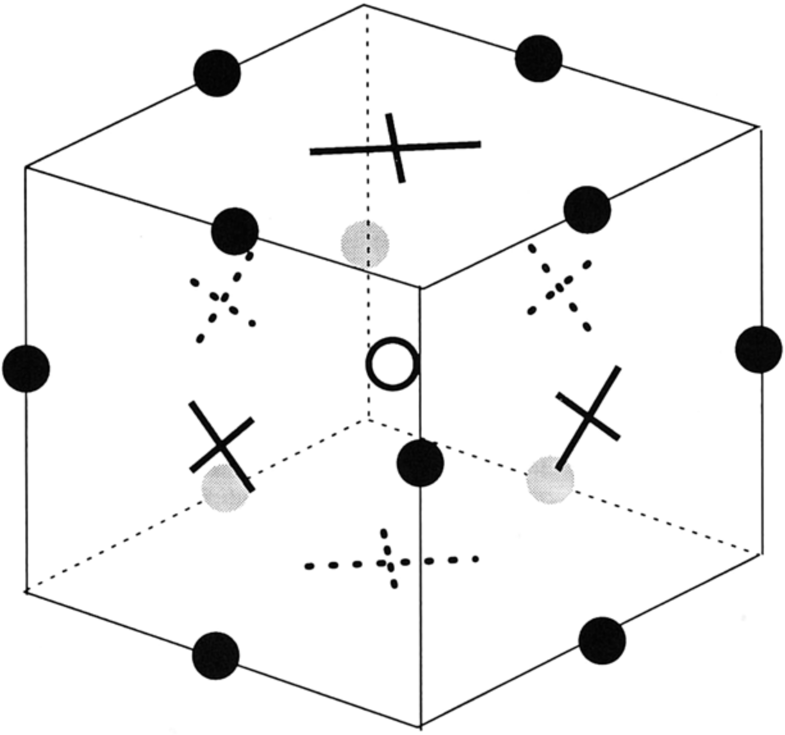

Fig. 1. The FCHC lattice. This is a representation of a three-dimensional projection of the unit cell of the four-dimensional lattice. The open circle at the center of the cubic box is a node of the lattice, and the filled circles and Xs are its 24 neighbors. Although the filled circles and Xs appear to be at different distances from the open circle, in four dimensions all the distances are the same. Each X corresponds to two neighbors which differ only in the fourth dimension; in this three-dimensional projection, they lie on top of each other. Gray circles and dashed Xs are on the far side of the unit cell. If the open circle is the origin, then the neighbors are all those locations with two coordinates equal to zero and two which are ± 1.

add up to an even number: for example, $(0, 0, 0, 0)$ and $(1, 0, -3, 0)$ are members of the lattice, but $(1, 2, 0, 0)$ is not. There are thus 2^{24} or 16,777,216 possible states at each node, so simply selecting the collision operator $\mathscr{C}$ is a substantial problem.(41) Our implementation of the two-phase, three-dimensional model uses an efficient operator developed by Somers, Rem, and Westland(42, 43) for the homogeneous fluid away from interfaces, although other operators could also be used.

3. THE TWO-PHASE MODEL

A variety of lattice-gas methods have been introduced to model multiphase flows,(18) including the two-species methods of Rothman and Keller,(15) Somers and Rem,(44, 29) and Chen *et al.*(45); in addition, the single-species method of Appert and Zaleski(46, 16, 17) separates spontaneously into regions of different density, simulating liquid and vapor phases. Our new model is most closely related to the Rothman and Keller model, with some influences from the related lattice-Boltzmann methods (for example, refs. 19 and 20). Earlier two-dimensional, two-species models have been applied to studies of complex flows in two dimensions(47–49) and have been extended to model three(31) and arbitrarily many(32) species in two dimensions. It is not clear, however, to what extent the results of two-dimensional simulations of multiphase flow can be applied to real, three-dimensional flows. For example, it is not possible in two dimensions for two species to span a box in both directions, while in three dimensions, both species can span a box in all directions simultaneously. Moreover, the dynamics of bubble breakage are entirely different in two and three dimensions. Thus it is necessary to develop a three-dimensional model to make meaningful simulations.

In the two-species models, an additional degree of freedom is assigned to each particle, a *color* which will be called *red* or *blue*. Particles carry color with them as they propagate, and color is conserved in collisions, just like mass and momentum. If a particle with velocity $\mathbf{c}_i$ is present at node $\mathbf{x}$ at time t, and if this particle is red, then $r_i(\mathbf{x}, t) = 1$ and otherwise, 0; if this particle is blue, then $b_i(\mathbf{x}, t) = 1$ and otherwise, 0. Consequently, $n_i = r_i + b_i$. The color states $\mathbf{r} = \{r_i\}_{i \in [1, 24]}$ and $\mathbf{b} = \{b_i\}_{i \in [1, 24]}$ defined in this way are used only for the propagation step. The collision rule (1) is applied to the state $\mathbf{n}$ without regard to color, and the new rules (defined below) which create phase separation and surface tension depend not on the velocity of each colored particle, but on the *color density* field

$$\phi(\mathbf{x}) = \sum_i (r_i(\mathbf{x}) - b_i(\mathbf{x})) \tag{4}$$

the *gradient* of the color density

$$\mathbf{f} = \sum_i \mathbf{c}_i \phi(\mathbf{x} + \mathbf{c}_i) \tag{5}$$

and the total number of red particles,

$$N_{\text{red}}(\mathbf{x}) = \sum_i r_i(\mathbf{x}) \tag{6}$$

If the color gradient **f** has a magnitude larger than some threshold, it is taken to indicate the local normal to an interface, and surface tension is created at this node. Surface tension can be expressed as a local anisotropy in the pressure: the pressure measured normal to the surface is larger than that tangential to the surface.(50) The pressure in a lattice gas is proportional to the density, so surface tension can be generated by placing particles preferentially in directions normal to the interface rather than tangential, while of course conserving momentum. Thus, we modify the post collision state $\mathbf{n}'$ to a new state $\mathbf{n}''$ by preferentially placing particles in directions as nearly parallel (and antiparallel) to **f** as possible, that is, by maximizing

$$\sum_i n_i'' \, |\hat{\mathbf{f}} \cdot \mathbf{c}_i| \tag{7}$$

where $\hat{\mathbf{f}} = \mathbf{f}/|\mathbf{f}|$, the unit vector in the direction of the color gradient. This maximization is approximated by reorienting pairs of oppositely directly particles (called *dumbbells*). Because these dumbbells have no net momentum, they can be reoriented freely, provided that they do not displace any other particles. The dumbbell scheme is the first of the two main technical innovations presented in this paper.

3.1. The Dumbbell Scheme

Reorienting. For each velocity $\mathbf{c}_i$ there is a diametric opposite, a $\mathbf{c}_j$ such that $\mathbf{c}_j = -\mathbf{c}_i$. Let us suppose that the set of velocities has been indexed such that $j = i + 12$ for all $i \in [1, 12]$; that is, $\mathbf{c}_{i+12} = -\mathbf{c}_i$. Then we will divide the post collision state $\mathbf{n}'$ into two symmetric parts, **L** and **H**, corresponding to the velocities with low and high indices, respectively:

$$\begin{aligned} L_i(\mathbf{n}') &= n_i' \\ H_i(\mathbf{n}') &= n_{i+12}' \end{aligned} \qquad \text{for} \quad i \in [1, 12] \tag{8}$$

It is convenient to describe the dumbbell method in terms of bitwise logical operations as follows:

$$\begin{aligned}
A_i \text{ and } B_i &= \begin{cases} 1 & \text{if } A_i = 1 \text{ and } B_i = 1 \\ 0 & \text{otherwise} \end{cases} \\
A_i \text{ or } B_i &= \begin{cases} 1 & \text{if } A_i = 1 \text{ or } B_i = 1 \\ 0 & \text{otherwise} \end{cases} \\
A_i \text{ xor } B_i &= \begin{cases} 1 & \text{if } A_i \neq B_i \\ 0 & \text{if } A_i = B_i \end{cases} \\
\text{not } A_i &= \begin{cases} 1 & \text{if } A_i = 0 \\ 0 & \text{if } A_i = 1 \end{cases}
\end{aligned} \tag{9}$$

The set of dumbbells $\mathbf{D}(\mathbf{n}') = \{D_i\}_{i \in [1,\,12]}$ is then all those directions i for which H_i and L_i are both equal to one:

$$D_i(\mathbf{n}') = H_i \text{ and } L_i \tag{10}$$

We also define the pairs of directions which contain unpaired particles:

$$U_i(\mathbf{n}') = H_i \text{ xor } L_i \tag{11}$$

It follows that $(D_i \text{ and } U_i) = 0$ for all i, that is, no pair of velocities can contain both a dumbbell and an unpaired particle.

A new set of dumbbells $\tilde{\mathbf{D}}$ is chosen to maximize

$$\sum_{i=1}^{12} \tilde{D}_i \, |\hat{\mathbf{f}} \cdot \mathbf{c}_i| \tag{12}$$

while conserving the number of dumbbells $(\sum_i \tilde{D}_i = \sum_i D_i)$ and using only those directions j with $U_j = 0$, so that the property

$$(\tilde{D}_i \text{ and } U_i) = 0$$

is preserved. This new set of dumbbells is used to construct a new state:

$$\begin{aligned}
\tilde{L}_i &= L_i \text{ and } (\text{not } D_i) \text{ or } \tilde{D}_i \\
\tilde{H}_i &= H_i \text{ and } (\text{not } D_i) \text{ or } \tilde{D}_i
\end{aligned} \tag{13}$$

that is, the new state is composed by removing the old dumbbells from the old state and adding the new ones. $\tilde{\mathbf{H}}$ and $\tilde{\mathbf{L}}$ together compose $\mathbf{n}''$, the state after collision and reorienting:

$$n_i'' = \begin{cases} \tilde{L}_i & \text{for } i \leqslant 12 \\ \tilde{H}_{i-12} & \text{for } i > 12 \end{cases} \tag{14}$$

Recoloring. Once the new state $\mathbf{n}''$ has been constructed, colors are reassigned to particles to minimize the diffusion of each species into the other. We define the *color flux*

$$\mathbf{q}(\tilde{\mathbf{r}}, \tilde{\mathbf{b}}) = \sum_i \mathbf{c}_i(\tilde{r}_i - \tilde{b}_i) \tag{15}$$

and choose $\tilde{r}_i$ and $\tilde{b}_i$ from those directions i which have $n_i'' = 1$, to maximize

$$\mathbf{q} \cdot \hat{\mathbf{f}}$$

while conserving the total number of red particles,

$$\sum_i \tilde{r}_i = N_{\text{red}}$$

Since each particle is either red or blue, labeling the red particles implicitly labels the blue particles.

Rather than carrying out the operations described above at every node and every time step, it is more efficient to precompute the results of these operations and store them in tables; then during the simulation, lengthy computation can be replaced with fast table lookups. However, these operations depend upon the direction of the gradient $\mathbf{f}$, and it is not practical to tabulate all the possible directions of the gradient. As detailed below, the symmetry of the lattice is used to reduce substantially the size of these tables, making the calculation practical.

3.2. Symmetric Tiling

The use of lattice symmetries proceeds by first breaking up the unit sphere into triangular *tiles*, all of the same size and shape but possibly of different orientation. These tiles, shown in Fig. 2, are constructed by drawing on the unit sphere the three great circles C_x, C_y, and C_z in the planes normal to the x, y, and z axes, respectively. The six great circles which bisect the angles between each pair of C_x, C_y, and C_z are also drawn. This divides the unit sphere into 48 tiles with many of the same symmetry properties as the FCHC lattice. One of the tiles is designated as the *archetype*, and tables are prepared to carry out the reorienting and recoloring operations for the four gradient directions given by the corners and the center of the archetypal tile. A table of lattice symmetry operations which transform each tile into the archetype is prepared as well.

Since the dumbbell method uses only the unit gradient vector $\hat{f}$, it suffices to determine the tile through which the gradient vector passes, and

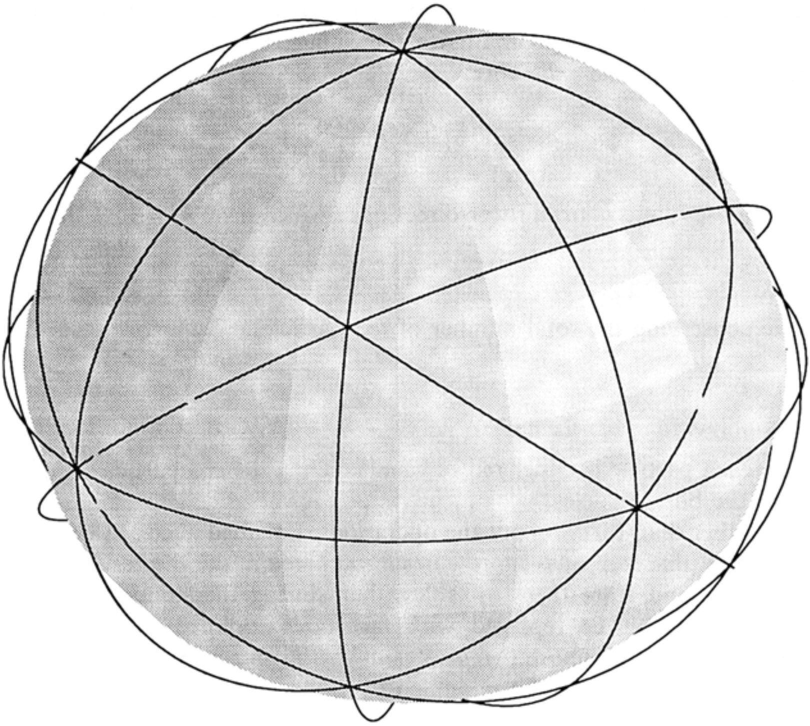

Fig. 2. The unit sphere is tiled with 48 identical triangles as shown, and unit gradients (i.e., $\mathbf{f}/|\mathbf{f}|$) are discretized to either a corner or the center of a triangle. The corners of the tiles are permutations of $(\pm 1, 0, 0)$, where eight tiles meet; permutations of $(\pm 1, \pm 1, 0)/\sqrt{2}$, where four tiles meet; and permutations of $(\pm 1, \pm 1, \pm 1)/\sqrt{3}$, where six tiles meet.

whether it passes nearer the center of the tile or one of its corners. Having found this tile, the appropriate lattice-symmetry operation $\mathscr{T}$ is used to move the gradient into the archetypal tile, and simultaneously to make the transformation $\mathbf{n}' \rightarrow \mathscr{T}\mathbf{n}'$. The nearest of the four archetypal gradients is used to find the appropriate reorientation and recoloring for the transformed state, yielding $\mathscr{T}\mathbf{n}''$ and $\mathscr{T}\tilde{\mathbf{r}}$. Finally, the inverse transformation $\mathscr{T}^{-1}$ is applied to these sets, returning them to the original orientation and yielding $\mathbf{n}''$ and $\tilde{\mathbf{r}}$.

The set of discrete orientations is large enough (it has 74 elements) that it successfully represents interfaces of arbitrary orientation, but it uses only four archetypes, which substantially reduces the memory needed to hold the tables.

In summary, the three-dimensional ILG algorithm consists of four steps, repeated endlessly: propagate, collide, reorient, and recolor, the latter two employing the symmetric tiling and the dumbbell method. In the earlier two-dimensional ILG models, the reorienting and recoloring were incorporated implicitly into the collision; here, on the other hand, they have been kept explicitly separate so that existing single-phase collision rules(43, 42) could be used unmodified, and also so that the strength of the surface tension and the antidiffusive flux may be adjusted independently of other model parameters.

4. PROPERTIES OF THE MODEL

A computer program has been constructed to implement the model as described, and various properties of the method have been measured from simulations. The first observation to make is that an initially uniform mixture does indeed undergo spontaneous phase separation (Fig. 3), as expected. The dynamics of phase separation has been examined in detail by Appert *et al.*(51) They conclude that the phase separation dynamics is consistent with theory, experiment, and other simulation methods, and they use the lattice gas to demonstrate the effect of hydrodynamics on the late stages of phase separation. Below, we discuss the surface tension of interfaces and isotropy of the phase domains.

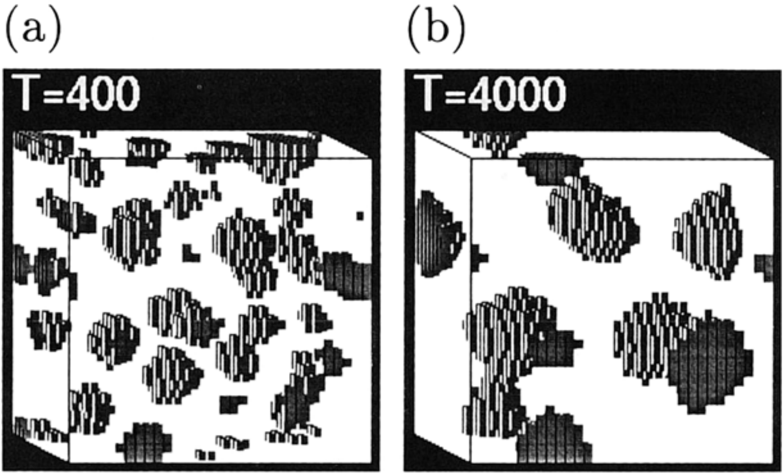

Fig. 3. Phase separation. The mixture was initialized with a uniform concentration of 10% red particles and 90% blue particles on a lattice of size 16 × 32 × 32; in these images, nodes with mostly blue particles are invisible and nodes with mostly red particles are gray. The images are at (a) 400 and (b) 4000 time steps after beginning separation.

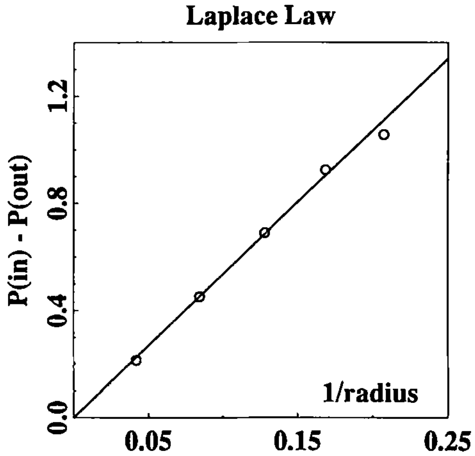

Fig. 4. The Laplace law is satisfied by phase domains. Circles are results from simulations, and the line is a best fit passing through the origin. Error bars on the data are within the circles. This case is for a density of 12 particles per node.

4.1. Surface Tension

If the lattice gas is initialized with a finite region of one species entirely surrounded by the other species, the smaller region is observed to relax to a spherical bubble. The pressure $p = \frac{1}{2}\sum_i n_i$ can be measured both inside and outside the bubble[30] and, as has been observed with two-dimensional

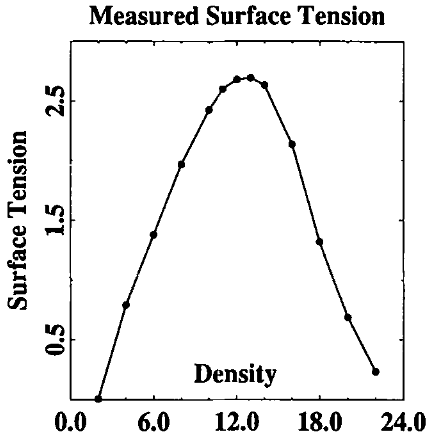

Fig. 5. The surface tension is strongest at densities near 12 particles per node, and decreases at higher and lower densities.

lattice-gas models,(15, 17, 29) the pressure inside exceeds that outside and the difference is inversely proportional to the radius of the bubble (see Fig. 4). This is just the behavior one would expect for a bubble with surface tension: Laplace's law, $P_{\text{in}} - P_{\text{out}} = \gamma/2R$, where R is the radius of the bubble and γ is the surface tension. Although there are theoretical predictions for γ in two-dimensional ILG models(30) and for two- and three-dimensional immiscible lattice-Boltzmann(19, 20) and liquid-gas(17) models, there is not yet a theoretical prediction of surface tension for this three-dimensional ILG model. The pressure difference is therefore used to measure the surface tension, which is found to vary with the density of the fluid as shown in Fig. 5, with its maximum value of $\gamma \approx 2.7$ at a density of 12 particles per node.

4.2. Isotropy

Some anisotropy of the surface tension is expected due to the inherent anisotropy of the lattice. Its effect on the shape of domains may be quantified by computing the *structure function*, an average over many independent simulations of the power spectrum of the color density field.

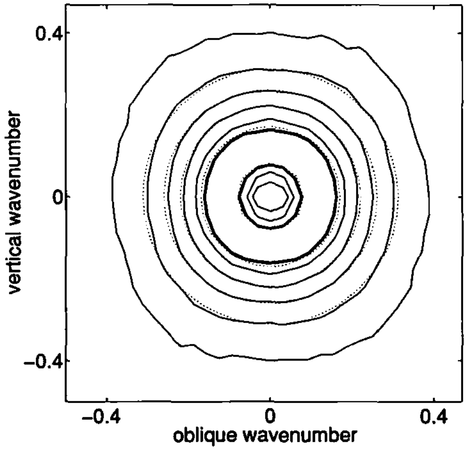

Fig. 6. A contour plot of the natural logarithm of an oblique slice [normal to (1, 1, 0)] through the structure function [defined in Eq. (16)] with $\Omega = 600$ at $t = 10$. The contours are at factors of e, from e^{-8} at the outermost to e^{-3} for the bold contours which enclose the maximum power of the spectrum. The dotted lines are exact circles for comparison. This slice has been chosen because it passes through all but one of the gradient archetypes (see Fig. 2) so it is most likely to reveal any anisotropy. Axis labels are in cycles per lattice unit.

That is, given Ω independent simulations with ϕ_j the color density field in the jth simulation, the structure function is

$$S(\mathbf{k}, t) = \frac{1}{\Omega} \sum_{j=1}^{\Omega} \left| \sum_{\mathbf{x}} \phi_j(\mathbf{x}, t)\, e^{-i\mathbf{k}\cdot\mathbf{x}} \right|^2 \tag{16}$$

If $S(\mathbf{k})$ has spherical symmetry, that is, if the structure function has the same value for all $\mathbf{k}$ with the same magnitude, then concentration variations are equally likely to occur in every direction and interfaces of every orientation are equally likely. Figure 6 is a two-dimensional slice through the three-dimensional structure function; slices in other directions look much the same, so the circular symmetry we see in the figure reflects spherical symmetry and, consequently, isotropic phase domains. However, surface tension may yet be significantly anisotropic. Indeed, surface tension must be strongly anisotropic before equilibrium phase domains depart significantly from the spherical.(17)

The time evolution of $S(\mathbf{k}, t)$ is studied in a separate paper,(51) where it is shown that it evolves in a manner consistent with theory and experiment, and is approximately self-similar in time.

5. SHEARED PHASE SEPARATION

We now turn to an application of this model to the flow of a two-phase mixture under shear. The effective rheology of a phase-separating mixture has been observed in experiments(27, 26) and predicted by theory.(7, 8) While the theory and experiment are known to be in qualitative agreement, a quantitative test of the theory requires a detailed knowledge of the interfacial geometry in the mixture, which is not available from experiment. In simulations, on the other hand, the interface geometry is readily available. In what follows, we simulate a mixture, observe its time-dependent effective viscosity and the interface geometry throughout the mixture, and compare these observations with the theoretical predictions. We find good agreement between the values calculated from the simulation and from the theory, and we find that the simulation behaves in qualitatively the same way as experimental systems.

5.1. Shear Flow in a Lattice Gas

In a simple shear flow, the velocity varies linearly in a direction orthogonal to the flow direction. For concreteness, let us consider a flow with $\mathbf{u} = -v\hat{\mathbf{z}}$ at $y=0$ and $\mathbf{u} = v\hat{\mathbf{z}}$ at $y = Y$, i.e.,

$$u_z(y) = v\left(2\frac{y}{Y} - 1\right) \qquad \text{for} \quad 0 \leqslant y \leqslant Y \tag{17}$$

Although this flow is simply described, it is not so easily generated in a lattice gas with periodic boundary conditions because, although the velocity field described in Eq. (17) is linear for $y=0$ to $y=Y$, it has a sudden jump between $y=Y$ and $y=0$. Earlier two-dimensional studies[47, 48] kept strictly periodic boundaries but imposed a nonlinear velocity field by driving the middle of the box upward and the outer edges downward. This produces a velocity field with kinks, and consequently deleterious effects. On the other hand, one might consider imposing nonperiodic boundary conditions in the shearing direction, for example, by imposing rigid walls moving at some velocity on either side of the simulation volume. This, too, may lead to problems, relating to the interaction of the fluids with the wall.

Such problems were resolved in molecular dynamics studies by Lees and Edwards,(52) who noted that periodic boundaries are equivalent to having an infinite array of identical images of the lattice stacked in all directions. When a particle leaves the lattice, it enters an image of the lattice just as a particle leaves a different image and enters the lattice. The Lees and Edwards boundary condition consists of moving the images continuously with respect to the lattice, so that a uniform velocity field extends across the lattice and all its images. In the lattice gas, this periodicity is achieved by two means: first, particles leaving the lattice through a shearing face are displaced transversely before reentering the lattice; second, the average velocity of particles is adjusted when they reenter the lattice so that the velocity of the particles with respect to the imposed flow remains the same.

Figure 7 illustrates the technique. When a particle (represented by the short arrow) leaves the $y=Y$ face of the lattice at time t, it reenters the $y=0$ face not at the same z, but at $z-2vt$, and with its vertical velocity reduced by $2v$, since the image to the right is moving at a speed $2v$ upward with respect to the lattice. Conversely, a particle (not shown) which leaves the $y=0$ face reenters the $y=Y$ face at $z+2vt$ with velocity increased by $2v$. Because the lattice gas is fully discrete, it is not possible to adjust the position and velocity by arbitrarily small increments. Instead, the position is adjusted by the closest integer number of lattice units. The velocity

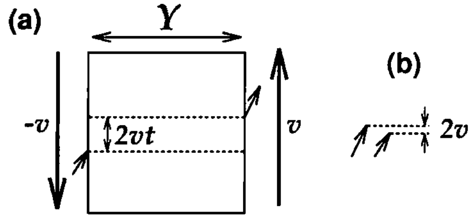

Fig. 7. Shearing boundary conditions in a periodic medium. (a) Maintaining a steady vertical velocity of $-v$ on the $y=0$ side of the box and v on the $y=Y$ side requires that particles leaving the right-hand face at time t reenter the left-hand face at a vertical position reduced by $2vt$, and with (b) vertical velocity reduced by $2v$.

adjustment is a little more complicated: it must be distributed as uniformly as possible over all the particles on each face at every time step.

5.2. Simulations

To simulate both growth and breakage of phase domains, both the properties of the fluid and the dimensions of the lattice must be chosen appropriately. Phase domains are expected to break when the capillary number $\mathrm{Ca} = \eta S a/\gamma \gtrsim 1$, where S is the strain rate and a is the characteristic radius of a drop.(53) In order to make Ca large enough within the constraints of the model, the calculations were performed at a density of 18 particles per node, which both reduces the surface tension (see Fig. 5) and increases the dynamic viscosity.(54) Further, the reorienting rule was applied only 5% of the time, and the recoloring rule only 50% of the time. These conditions give $\gamma \approx 0.011$ and $\eta \approx 1.2$, so that bubbles could be stretched and broken while keeping the velocity small enough ($u \lesssim 0.1$) that the lattice gas could accurately represent the flow.

We use a lattice of size $32 \times 16 \times 160$ with y the shear direction and z the flow direction for the measurements of effective viscosity. The system is initialized with a single stable phase (by labeling all the particles with the same color) and driven with a steady shear for a time so as to set up a steady state. Then the conditions are suddenly changed so that the single phase becomes unstable (by instantaneously labeling some fraction of the particles, at uniformly distributed, random locations with the other color) and phase separation is observed. Concurrent with the phase separation, the effective viscosity of the fluid is measured at each time step over the entire lattice. To make this measurement, the horizontal flux of vertical momentum is averaged over the entire simulation volume, excluding the outer planes where the forcing is imposed; the ratio of this flux to the strain rate then gives the effective dynamic viscosity of the fluid.

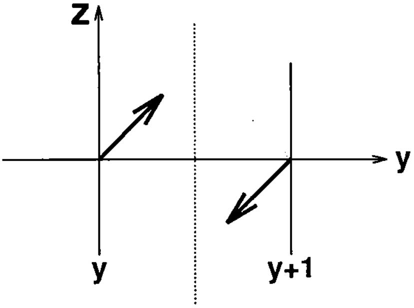

Fig. 8. The momentum flux across the dotted line has a positive contribution from particles with velocities represented by the black arrows, and a negative contribution from particles with velocities represented by the gray arrows. Summing such contributions over all x and z values on either side of the plane represented by the dotted line yields the total flux of vertical momentum across the plane.

Specifically, consider the flux of vertical momentum between planes of nodes at y and $y+1$ (Fig. 8). Both upward momentum transported in the increasing-y direction [particles with velocity $\mathbf{c}_p=(0, 1, 1)$ at y] and downward momentum transported in the decreasing-y direction [velocity $\mathbf{c}_{p+12}=(0, -1, -1)$ at $y+1$] correspond to positive momentum flux; negative momentum flux corresponds to $\mathbf{c}_n=(0, 1, -1)$ at y and $\mathbf{c}_{n+12}$ at $y+1$. The net flux between the two planes in the direction of increasing velocity is then

$$\mathscr{F}(y)=\sum_{x,z} n_p(x, y, z)+n_{p+12}(x, y+1, z)-[n_n(x, y, z)+n_{n+12}(x, y+1, z)] \tag{18}$$

The average shear stress on the fluid is then

$$\sigma_{yz}=\frac{1}{Y-3}\sum_{y=2}^{Y-2}\mathscr{F}(y) \tag{19}$$

and the effective dynamic viscosity is thus

$$\eta_{\text{eff}}=\frac{\sigma_{yz}}{S} \tag{20}$$

The planes at $y=1$ and $y=Y$, the faces of the lattice, are not included, because the states on these faces are artificially controlled by the boundary conditions.

5.3. Observations and Comparison with Experiment

Early in the phase separation, domains are too small to be influenced by the strain, and so remain essentially spherical; as the domains grow larger, they begin to be stretched and to break and merge, as expected. Figure 9 shows the early and late stages of the phase separation; the geometry of this simulation was chosen for ease of visualization, so it is not the same as that used for effective viscosity measurements. Eventually the domains converge to a single long thread, which should be considered an artifact of the periodic boundary conditions in the vertical direction—although similar threads are observed in experiments.(26) The effective viscosity is observed to rise rapidly and then to decay gradually to a steady state value which is larger than that of the pure fluid (Fig. 10). The effective viscosity, both at the maximum and at steady state, increases with increasing concentration (Fig. 11) and *decreasing* strain rate (Fig. 12). These observations are in qualitative agreement with experiments,(55, 27, 26) though the strain-rate dependence seems counterintuitive.

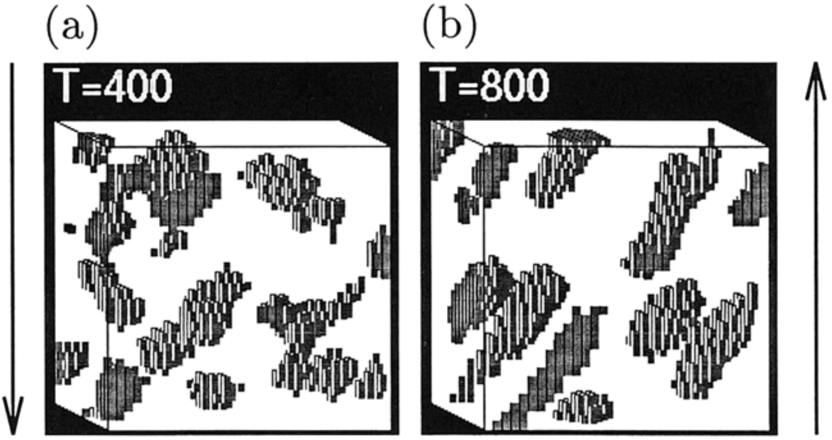

Fig. 9. Growth under shear. The velocity field in each image points down on the left and up on the right. As the phase domains grow larger, they are more strongly affected by the imposed strain field. The images are at (a) 400 and (b) 800 time steps after the beginning of phase separation. At early times, the domains are not distinguishable from the unforced case of Fig. 3. The dimensionless strains (for comparison with Fig. 10) are (a) $Ct = 2.58$ and (b) 5.16 and the concentration is 10% red. The velocities on the left and right sides of the box are -0.1 and 0.1 lattice units per time step, respectively, on a lattice with the same dimensions as in Fig. 3 (i.e., $Y = 32$), so the strain rate is 0.00645 (time step)$^{-1}$.

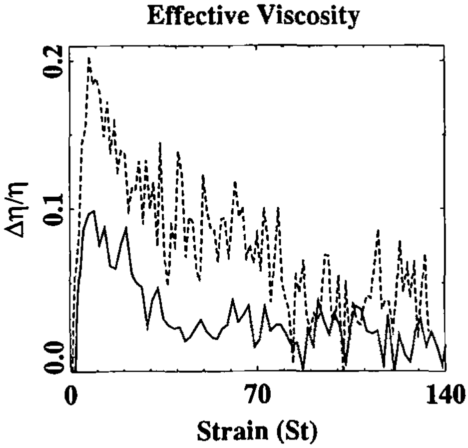

Fig. 10. The effective viscosity of the mixture increases abruptly when phase separation starts, then decreases gradually to a steady state. The points are averages over 100 time steps in a single simulation with 20% concentration and a strain rate of 0.02 $(\text{time step})^{-1}$ (solid line) or 0.0133 $(\text{time step})^{-1}$ (dashed line). The time has been scaled by the strain rate so that the two cases can be compared at the same dimensionless strain.

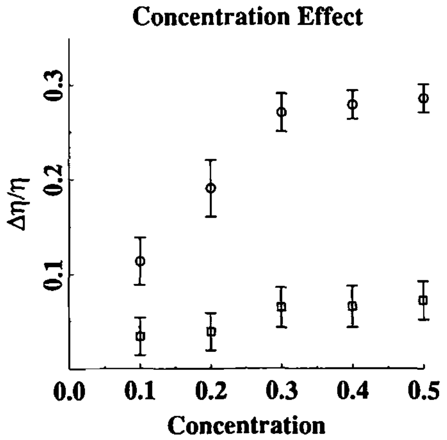

Fig. 11. Both maximum (circles) and steady-state (squares) viscosities increase with increasing concentration, which is consistent with the Doi–Ohta theory.[8] These data are for simulations with strain rate 0.0133 $(\text{time stepp})^{-1}$.

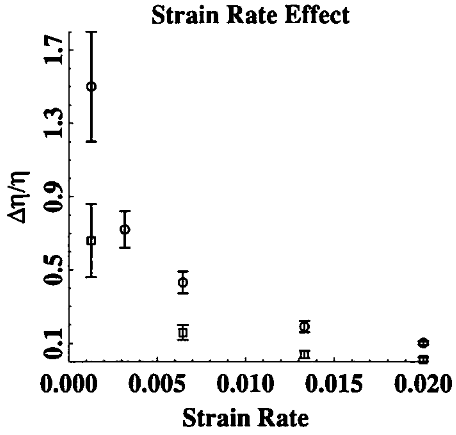

Fig. 12. Both the maximum (circles) and steady-state (squares) viscosities increase with decreasing strain rate. The simulation with the second-slowest strain rate did not come to a steady state, so was omitted. The Doi–Ohta theory(8) predicts that the steady-state viscosity should be independent of strain rate.

5.4. Discussion and Comparison with Theory

Broadly speaking, the observed viscosity enhancement must be due to some dissipative process which takes place in the phase-separating mixture, but which is absent in a pure fluid. The obvious candidate is the elastic energy which is stored in a phase domain as it is stretched, and which is dissipated when the domain finally breaks. Onuki(7) has developed a theory which predicts that the relative enhancement of the effective viscosity of a mixture should depend on the amount and orientation of interfaces per unit volume:

$$\frac{\Delta\eta}{\eta} = \frac{\gamma A}{-\eta S} \langle \nu_y \nu_z \rangle_b \qquad (21)$$

where $\Delta\eta = \eta_{\text{eff}} - \eta$, $A = (1/V) \int_V 1 \, ds$ (the interfacial area per unit volume), ν_α is the α-component of the unit normal to an interface, and $\langle \lambda \rangle_b = (1/V) \int_V \lambda \, ds/A$ is the average of a quantity λ over all the interfaces in a sample of volume V. Doi and Ohta(8) extended this theory by making a continuum approximation to the average interfacial quantities and deriving the responses of these continua to macroscopic flow. According to the Doi–Ohta theory, the steady-state effective viscosity should be independent of strain rate. The simulation, on the contrary, shows an increase of viscosity with decreasing strain rate (Fig. 12), which is at least partially borne out by experiment.(26) This discrepancy may be a consequence of the finite size of the simulation.

The interface integral $\langle v_y v_z \rangle_b$ may be approximated from the simulation as the sum over the entire lattice

$$\langle v_y v_z \rangle_b = \frac{1}{AV} \sum_{\mathbf{x}} f_y(\mathbf{x})\, f_z(\mathbf{x}) \tag{22}$$

with V the volume of the lattice and f_α the αth component of $\hat{\mathbf{f}}$. It is then a simple matter to calculate the Onuki prediction (21) and compare it with the measured values. Figure 13 shows the results for a case with concentration 20% and strain rate 0.013 (time step)$^{-1}$, although other cases were qualitatively similar. The theory consistently predicts the observed effective viscosity within 10–20% regardless of concentration or strain rate. Because the prediction is consistently low regardless of these simulation parameters, it seems likely that the discrepancy is due to some systematic error. The most obvious potential error is in the value of the surface tension: differences of 10–20% are commonly observed among theoretical predictions and different measurement methods.(30) Another possible source of error could be the approximation of an integral over a small volume by a sum over the entire lattice in Eq. (22). This same approximation was used in the earlier two-dimensional lattice-gas calculation,(48) wherein a discrepancy of the same sign and about the same magnitude was observed.

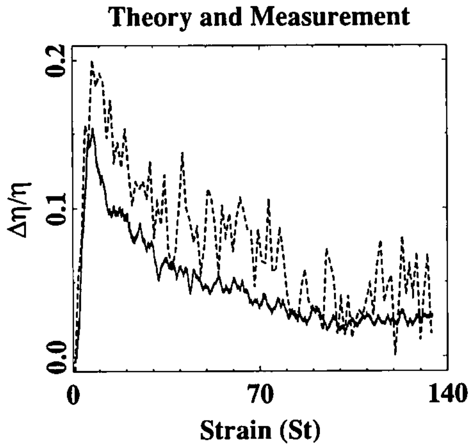
Theory and Measurement

Fig. 13. The Onuki theory,(7) (solid line) predicts the time-dependent effective viscosity (dashed line) within 10–20%, regardless of concentration or strain rate. This example is for concentration 20% and strain rate 0.013 (time step)$^{-1}$.

6. CONCLUSIONS

A new immiscible lattice-gas model in three dimensions has been described and characterized. It is based upon ideas developed in two-dimensional immiscible lattice gases and lattice-Boltzmann models, and offers a straightforward extension to three or more fluids. The new "dumbbell method" generates strong surface tension by reorienting oppositely directed pairs of particles, and the new scheme to discretize gradients using the isometries of the lattice provides both a high degree of symmetry and an efficient implementation.

The model has been applied to measurements of the effective viscosity of phase-separating mixtures undergoing steady, simple shear, which required the application of a new periodic boundary condition with shear. The time-dependent effective viscosity is found to be in good qualitative agreement with both theoretical predictions and experimental measurements. This new model appears to be a valid means to simulate the complex flow of binary fluid mixtures at low speeds. Preliminary investigations are underway to model two-phase flow in porous media using this method.

ACKNOWLEDGMENTS

The authors would like to thank J. Somers and P. C. Rem of Koninklijke/Shell-Laboratorium, Amsterdam, for generously making available to us their efficient collision tables for the FCHC lattice gas. Acknowledgment is made to the donors of the Petroleum Research Fund, administered by the American Chemical Society, for partial support of this research. The research was also supported in part by the sponsors of the MIT Porous Flow Project and by NSF grant EAR-9218819.

REFERENCES

1. L. A. Utracki, *Polymer Alloys and Blends* (Hanser Publishers, 1990).
2. G. I. Taylor, *Proc. R. Soc. Lond. A* **138**:41–48 (1932).
3. F. D. Rumscheidt and S. G. Mason, *J. Colloid Sci.* **16**:238–261 (1961).
4. V. G. Levich, *Physicochemical Hydrodynamics* (Prentice-Hall Englewood Cliffs, New Jersey, 1962).
5. T. Gillespie, The effect of concentration on the viscosity of suspensions and emulsions, in *Rheology of Emulsions* (Macmillan, (1963), pp. 115–124.
6. S. Torza, R. G. Cox, and S. G. Mason, *J. Colloid Interface Sci.* **2**:395–411 (1972).
7. A. Onuki, *Phys. Rev. A* **35**:5149 (1987).
8. M. Doi and T. Ohta, *J. Chem. Phys.* **95**:1242–1248 (1991).
9. B. V. Boshenyatov and I. V. Chernyshev, *Fluid Mech. Sov. Res.* **20**:124–129 (1991).
10. D. Beysens, F. Perrot, and T. Baumberger, *Physica A* **204**:76–86 (1994).

11. D. A. Drew, *Annu. Rev. Fluid Mech.* **15**:261 (1983).
12. B. Lafaurie, C. Nardone, R. Scardovelli, S. Zaleski, and G. Zanetti, *J. Comput. Phys.* **113**:134–147 (1994).
13. T. Koga and K. Kawasaki, *Physica A* **196**:389–415 (1993).
14. S. Puri and B. Dünweg, *Phys. Rev. A* **45**:R6977–R6980 (1992).
15. D. H. Rothman and J. Keller, *J. Stat. Phys.* **52**:1119 (1988).
16. C. Appert and S. Zaleski, *Phys. Rev. Lett.* **64**:1 (1990).
17. C. Appert and S. Zaleski, *J. Phys. II France* **3**:309–337 (1993).
18. D. H. Rothman and S. Zaleski, *Rev. Mod. Phys.* **66**:1417–1479 (1994).
19. A. K. Gunstensen, D. H. Rothman, S. Zaleski, and G. Zanetti, *Phys Rev. A.* **43**:4320–4327 (1991).
20. A. K. Gunstensen and D. H. Rothman, *Europhys. Lett.* **18**(2):157–161 (1992).
21. D. Grunau, S. Chen, and K. Eggert, *Phys. Fluids A* **5**:2557–2562 (1993).
22. F. J. Alexander, S. Chen, and D. W. Grunau, *Phys. Rev. B* **48**:634 (1993).
23. X. Shan and H. Chen, *Phys. Rev. E* **47**:1815–1819 (1993).
24. T. Toffoli and N. Margolus, *Physica D* **47**:263–272 (1991).
25. C. Adler, B. Boghosian, E.G. Flekkøy, N. Margolus, and D. H. Rothman, *J. Stat. Phys.*, this issue.
26. K. Hamano, T. Ishii, M. Ozawa, J. V. Sengers, and A. H. Krall, *Phys. Rev. E* **51**:1254–1262 (1995).
27. A. H. Krall, J. V. Sengers, and K. Hamano, *Phys. Rev. Lett.* **69**:1963–1966 (1992).
28. B. Khuzhaerov, *J. Eng. Phys.* **1991**:1564–1570.
29. P. C. Rem and J. A. Somers, Cellular automata on a transputer network, in *Discrete Kinetic Theory, Lattice-Gas Dynamics, and Foundations of Hydrodynamics*, R. Monaco, ed. (World Scientific, singapore, 1989), p. 268.
30. C. Adler, D. d'Humières, and D. H. Rothman, *Jour. Phys. I France* **4**:29-46 (1994).
31. A. K. Gunstensen and D. H. Rothman, *Physica D* **47**:47–52 (1991).
32. D. H. Rothman and L. P. Kadanoff, *Comput. Phys.* **8**:199–204 (1994).
33. U. Frisch, B. Hasslacher, and Y. Pomeau, *Phys. Rev. Lett.* **56**:1505 (1986).
34. U. Frisch, D. d'Humières, B. Hasslacher, P. Lallemand, Y. Pomeau, and J.-P. Rivet, *Complex Systems* **1**:648 (1987).
35. G. Zanetti, *Phys. Rev. A* **40**:1539 (1989).
36. L. Kadanoff, G. McNamara, and G. Zanetti, *Phys. Rev. A* **40**:4527 (1989).
37. S. Wolfram, *J. Stat. Phys.* **45**:471 (1986).
38. A. K. Gunstensen and D. H. Rothman, *Physica D* **47**:53–63 (1991).
39. D. d'Humières, P. Lallemand, and U. Frisch, *Europhys. Lett.* **2**:291 (1986).
40. H. S. M. Coxeter, *Regular Polytopes* (Dover, New York, 1973).
41. M. Hénon, *Complex Systems* **1**:475–494 (1987).
42. G. Westland, Optimizing a reduced collision table for the FCHC-lattice gas automaton, Master's thesis, State University of Utrecht (April 1991).
43. J. A. Somers and P. C. Rem, Obtaining numerical results from the 3D FCHC-lattice gas, in *Numerical Methods for the Simulation of Multi-Phase and Complex Flow*, T. M. M. Verheggen, ed. (Springer-Verlag, Berlin, 1992), pp. 59–78.
44. J. A. Somers and P. C. Rem, *Physica D* **47**:39–46 (1991).
45. S. Chen, G. D. Doolen, K. Eggert, D. Grunau, and E. Y. Loh, *Phys. Rev. A* **43**:7053–7056 (1991).
46. C. Appert, D. H. Rothman, and S. Zaleski, *Physica D* **47**:85–96 (1991).
47. D. H. Rothman, *Phys. Rev. Lett.* **65**:3305 (1990).
48. D. H. Rothman, *Europhys. Lett.* **14**:337–342 (1991).
49. D. H. Rothman, *J. Geophys. Res.* **95**:8663 (1990).

50. J. Rowlinson and B. Widom, *Molecular Theory of Capillarity* (Clarendon Press, Oxford, 1982).
51. C. Appert, J. F. Olson, D. H. Rothman, and S. Zaleski, *J. Stat. Phys.*, this issue.
52. A. W. Lees and S. F. Edwards, *J. Phys. C: Solid State Phys.* **5**:1921–1929 (1972).
53. J. M. Rallison, *Annu. Rev. Fluid Mech.* **16**:45–66 (1984).
54. M. Hénon, *Complex Systems* **1**:763–789 (1987).
55. A. H. Krall, J. V. Sengers, and K. Hamano, *Int. J. Thermophys.* **10**:309 (1989).